Soft Matter

ROYAL SOCIETY
OF CHEMISTRY

PAPER
Farhang Radjai *et al.*
Dynamic compaction of cohesive granular materials: scaling
behavior and bonding structures

PAPER

Dynamic compaction of cohesive granular materials: scaling behavior and bonding structures†

Max Sonzogni, [ID] [ab] Jean-Mathieu Vanson, [ID] [a] Katerina Ioannidou, [ID] [b]
Yvan Reynier, [c] Sébastien Martinet [ID] [c] and Farhang Radjai [ID] *[b]

The compaction of cohesive granular materials is a common operation in powder-based manufacture of many products. However, the influence of particle-scale parameters such as bond strength on the packing structure and the general scaling of the compaction process are still poorly understood. We use particle dynamics simulations to analyze jammed configurations obtained by dynamic compaction of sticky particles under a fixed compressive pressure for a broad range of system parameter values. We show that relative porosity, representing the relative importance of porosity with respect to its minimum and maximum values, is a unique function of a modified cohesion number that combines adhesion force, confining pressure, and particle size, as well as contact stiffness, which is often assumed to be ineffective but is shown here to play an essential role in compaction. An asymmetric sigmoidal form based on two power laws provides an excellent fit to the data. The statistical properties of the bond network reveal self-balanced force structures and an exponential fall-off of the number of both tensile and compressive forces. Remarkably, the properties of the bond network depend on the cohesion number rather than the modified cohesion number, implying that similar bond network characteristics are compatible with a broad range of porosities mainly due to the effect of contact stiffness. We also discuss the origins of data points escaping the general scaling of porosity and show that they reflect either finite system size or rigid confining walls.

1 Introduction

Granular materials represent a ubiquitous form of solid matter in nature and a major component of the manufacturing process in several industries. The mobility of grains and their versatile interactions underlie the ability of granular materials to undergo diverse mechanical and chemo-physical transformations in response to external forces and environmental changes. These transformations are strongly coupled with a change of porosity or volume, which for this reason plays a key role in all granular processes.[1,2] For example, the compaction and gradual consolidation of sediments deposited in lakes and oceans are at the origin of sedimentary rocks such as sandstone, limestone, and shale.[3] The compaction of fine cohesive particles in response to mechanical stress or vibrations is also one of the most

common operations in powder metallurgy, the ceramic industry, and the pharmaceutical industry for the production of stable agglomerates of desired composition, shape, strength, and porosity. Some examples are pharmaceutical pills,[4–8] nuclear fuel pellets,[9,10] detergent tablets,[11,12] titanium compact tools,[13–15] and Li-ion battery electrodes.[16–20]

The physics of volume change in granular materials is complex due to the interplay of the concurrent effects of mutual particle exclusions, collisional energy dissipation, friction, bond forces, and collective dynamics involving arching and force correlations.[21,22] The Reynolds dilatancy (volume change by shear), the sensitive dependence of the packing fraction on the confinement strategy, and the highly inhomogeneous distribution of local porosities as a result of shear-banding and wall boundary conditions are among well-known features that heavily bear on the practical handling of granular materials and raise fundamental issues about the microstructural origins and controllability of volume changes.[23–29] Although experimental methods are often designed to meet the specific challenges and types of materials of interest in each field, such common features prompt also the basic question of whether a universal or an inherent volume-change behavior can be extracted.

[a] CEA, DES, IRESNE, DEC, Cadarache, F-13108 Saint-Paul-lez-Durance, France
[b] LMGC, CNRS, University of Montpellier, 34090 Montpellier, France.
  E-mail: franck.radjai@umontpellier.fr
[c] Université Grenoble Alpes, CEA, Liten, DEHT, 38000 Grenoble, France
† Electronic supplementary information (ESI) available. See DOI: https://doi.org/10.1039/d3sm01116j

This question has been so far mostly addressed in the case of cohesionless granular materials in soil mechanics.[2,30] A nearly logarithmic dependence of the porosity on the confining pressure or on the number of vibration cycles has been evidenced.[2,26,31,32] This scaling holds within two limits of porosity corresponding to the lowest and highest porosities that can be reached by applying an assembling procedure to a granular material. The lowest porosity represents the densest random packing state that is compatible with steric exclusions whereas the highest porosity is a property of the loosest state that is compatible with the static equilibrium and stability of the packing. Most work on cohesive granular materials concerns compaction by ballistic aggregation or under the action of a compressive pressure.[23,33,34] A remarkable effect of adhesion between particles is to increase the range of accessible porosities as compared to cohesionless materials.[35,36] Indeed, much higher porosities can be reached due to the stabilizing effect of tensile forces on the particles. However, in most experiments reported on powder compaction only a limited range of porosities is considered; the main concern often being the mechanical strength induced by compaction together with specific target functionalities such as specific surface or permeability rather than porosity alone.[37-40]

Several different compaction laws have been proposed in the case of cohesive powders including the logarithmic dependence of the porosity on the applied pressure for quasi-static compaction and the power-law dependence on the cohesion number for dynamic compaction.[5,20,24] However, the particle-scale physical mechanisms deriving the compaction process are not the same for all processes. At low compressive stresses, the compaction is mainly due to diffusive-like motions, aggregation, and rearrangements of the particles whereas at high compressive stresses, the porosity increases also as a result of plastic particle shape change and breakage. Very low levels of porosity can be achieved in the latter case.[18,41-43] It is also important to distinguish the primary compaction of a granular material as a consequence of the preparation method, such as filling a die, from the secondary compaction, which is applied with the intension of reducing porosity or enhancing the tensile strength of the compact.

Beyond many insights provided by compaction experiments, a systematic understanding of the microstructural mechanisms that underlie the compaction behavior of cohesive granular materials may be achieved by means of particle dynamics simulations based on the discrete element method (DEM).[44-48] In this method, the classical equations of motion of rigid particles are incrementally integrated by accounting for the interactions between particles. For example, 2D simulations of the compaction of sticky particles with and without rolling resistance were carried out to analyze the influence of the assembling protocol on the resulting microstructures.[23,49] In these simulations, a primary process of ballistic aggregation was first applied to obtain a stable packing with high porosity. Then, the packing was compressed by a quasistatic stepwise increase of isotropic pressure under periodic boundary conditions. The simulations reveal the fractal structure of the packing below a correlation length on the order of a few diameters (fractal blobs). During compaction, loose structures collapse as the tensile strength of contacts is overcome by the externally imposed forces. It is found that the consolidation process is governed by the reduced pressure p^* defined as the ratio of the applied pressure to the internal cohesive stress. A nearly logarithmic dependence of porosity on the reduced pressure is observed as in experiments, followed by a power-law fall-off down to the porosity of a cohesionless material. A similar compaction process was simulated in 3D and similar results were obtained.[50,51] There are few simulations accounting for particle shape change. A new algorithm coupling material point method (MPM) for the simulation of particle deformation with DEM for frictional contact interactions in 2D was able to simulate the compaction of a collection of soft disks down to a porosity close to zero.[43] Interestingly, the logarithmic scaling of porosity in these simulations was found to hold when compaction enters a stage of particle deformation without rearrangements. Similar simulations in 3D by coupling DEM with finite elements were recently reported.[42]

In this paper, we employ 3D particle dynamics simulations to analyze the compaction of a collection of sticky spheres enclosed inside a box whose walls are subjected to a constant isotropic compressive pressure. The particles are assumed to be rigid and unbreakable so the compaction is merely due to particle aggregation and rearrangement. In contrast to quasi-static simulations, where the pressure is increased in a step-wise manner after an initial aggregation process, the compaction process in our simulations is a consequence of the action of the confining pressure without step-wise control and equilibration of the packing. In this sense, our simulations are fully dynamic and represent the natural process of primary compaction under load. We also apply a small kinetic agitation to the particles to randomize the initial particle positions. Hence, the compaction is a consequence of diffusion, ballistic aggregation, and collective rearrangements of the particles.

We are interested in the characteristics of the packing and its internal structure as a function of adhesion force, compressive pressure, particle size, and contact stiffness. Recent simulations of sheared cohesive granular materials evidenced an unexpected influence of contact stiffness on the location of shear bands.[52,53] Previous simulations of the fluidization of cohesive powders have also revealed a significant influence of contact stiffness on the onset of fluidization, but this effect has never been studied in the compaction process.[54,55] As we shall see, the combination of contact stiffness with the cohesion number, defined as the ratio of adhesive stress to the confining stress and corresponding to the inverse of reduced pressure, leads to a new dimensionless parameter that properly scales the porosity. Nevertheless, as we shall see, the bonding structure is more appropriately scaled by the cohesion number, implying that packings with a wide range of porosities can have similar bond networks.

An important goal of this work is to clarify the effects of rigid walls, which are essential elements of most applications and are expected to play a major role in cohesive granular materials. For this reason, periodic boundary conditions were avoided. The walls and their motion with a finite mass under the action

of the applied pressure lead to strong inhomogeneity of the bonding structure at very low and very high pressures. Such inhomogeneities are often observed in cohesive powders and we will show that, while the average porosity is basically well scaled by system parameters, the presence of the walls leads to average porosities that escape the proposed scaling.[26]

In the following, we first describe the simulation method with a focus on the force laws and the characteristics of the simulated system in Section 2. In Section 3, we present a detailed parametric study of porosity as a function of system parameters. We consider the scaling of the data with a modified cohesion number, the origin of the influence of contact stiffness, the dependence of the highest porosity on system parameters, the effect of the damping parameter, the influence of wall mass and initial porosity, and the functional form of the collapsed porosity data on the modified cohesion number. In Section 4, we characterize the bonding structures in terms of connectivity and force transmission, as well as the origins of the data points escaping the general scaling proposed. Finally, in Section 5, we conclude with a summary of the main findings of this work and open issues for further investigation.

2 Methodology

2.1 Force laws

For simulations, we used an in-house code based on DEM (code called Rockable; see ref. 56). The classical velocity-Verlet time-stepping scheme of the equations of motion and contact detection procedures are used in this code.[57] The total interaction force f between two particles is the sum of normal and tangential components f_n and f_t, respectively:

$$f = f_n n + f_t, \quad (1)$$

where n is the contact normal. The directions of n and f_t are generally defined to point from a neighboring particle to the particle considered. The interaction force is a function of the overlap δ_n, assumed to be negative when contact occurs, and cumulative tangential displacement δ_t.

We used an elasto-adhesive contact law, in which the normal force is the sum of a linear elastic repulsion force $f_n^e = -k_n \delta_n$, where k_n is the normal stiffness, and a constant adhesion force $-f_c$:

$$f_n = \begin{cases} f_n^e - f_c = -k_n \delta_n - f_c & \text{for } \delta_n < 0, \\ 0 & \text{for } \delta_n \geq 0, \end{cases} \quad (2)$$

The graph of this force law is plotted as shown in Fig. 1(a).

The adhesion force f_c is assumed to represent the vdW (van der Waals) force, which is the main source of bonding for fine particles. The vdW force between two particles is given by

$$f_w = \frac{24Ad}{h^2}, \quad (3)$$

where A is the Hamaker constant, d is the particle radius, and h is the gap distance between the surfaces of the two particles. As the force falls off rapidly with distance, it can be set with a good
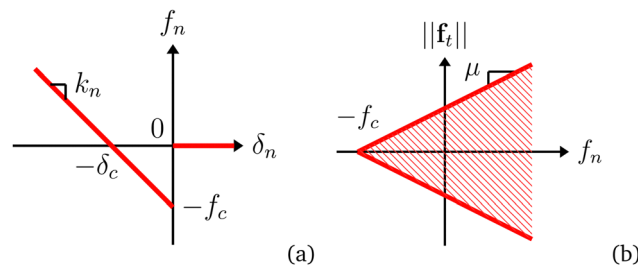

Fig. 1 Graphs of (a) normal force law (eqn (2)) and (b) Coulomb criterion (eqn (7)).

approximation equal to its value at the minimal distance h_0 allowed by surface roughness:

$$f_c \simeq \frac{Ad}{24h_0^2}. \quad (4)$$

Such a constant adhesion force acting only at the contact between two particles may be coined as a simple adhesion law. Equivalently, we may consider that f_c is the pull-off force required to break the cohesive bond:[58]

$$f_c = \frac{3}{4}\pi\gamma d, \quad (5)$$

where $\gamma = A/(18\pi h_0^2)$ is the surface energy.

In the numerical model, we assume that f_c is independent of the overlap between particles. Second-order effects related to the variations of the adhesion force with the overlap or gap[54,59] can be more suitably evaluated by comparison with the simple adhesion law. In the absence of external forces acting on two touching particles, the adhesion force is exactly balanced by the elastic repulsive force so that $f_n = 0$ and the overlap at equilibrium is given by

$$\delta_c = -\frac{f_c}{k_n}. \quad (6)$$

When two particles are pulled apart from this equilibrium configuration, a tensile force is mobilized ($f_n < 0$) and increases in absolute value up to $-f_n = f_c$ for $\delta = 0$, where the cohesive bond fails. During compaction, only compressive pressure is exerted on the sample but tensile forces develop in the contact network as a consequence of forced collective particle rearrangements.

For the tangential force, we used a linear elastic law together with a Coulomb dry friction criterion:

$$f_t = \begin{cases} -k_t \delta_t & \text{for } \|f_t\| \leq \mu(f_n + f_c), \\ -\mu(f_n + f_c)\dfrac{\dot{\delta}_t}{\|\dot{\delta}_t\|} & \text{otherwise,} \end{cases} \quad (7)$$

where μ is the friction coefficient and k_t is the tangential stiffness. Throughout this work, we set $k_t = 1.5k_n$. We checked that the ratio k_t/k_n has a negligibly small influence on the compaction and porosity of bonding structures although its role in shear simulations may be significant. Note also that, as compared to the Coulomb criterion $\|f_t\| \leq \mu f_n$ for cohesionless contacts; here, the Coulomb cone is shifted to account for the adhesion force added to the normal force, as shown in Fig. 1(b).[48,60] This means that

only the repulsive part $f_n^e = f_n + f_c$ of the normal force comes into play.

For energy dissipation, in addition to frictional sliding and bond breaking as two natural mechanisms of dissipation, we assume inelastic collisions with a restitution coefficient $\varepsilon_n < 1$. In cohesionless contacts, the value of ε_n is controlled by adding a viscous normal force f_n^v to the elastic and adhesion forces:

$$f_n^v = -2\alpha_n\sqrt{k_n m}\dot{\delta}_n, \qquad (8)$$

where m is the particle mass. With this parametrization of the damping force, α_n is simply given by

$$\alpha_n = -\frac{\ln(\varepsilon_n)}{\sqrt{\ln^2(\varepsilon_n) + \pi^2}}. \qquad (9)$$

The value of ε_n represents the inelasticity of the contact independently of adhesion. As we shall see in Section 3.2, the effective restitution coefficient for cohesive contacts is lower and can be calculated as a function of both α_n and f_c. In particular, for a range of impact velocities below a critical velocity depending on f_c, the effective restitution coefficient vanishes and colliding particles aggregate.[61] In nearly all simulations, we set $\varepsilon_n = \sqrt{0.2}$, corresponding to $\alpha_n \simeq 0.25$. In Section 3.5, we will discuss the effect of ε_n on the scaling of porosity. Finally, we set the cohesionless tangential damping to zero. This implies that the aggregation of colliding particles is controlled only by normal damping.

2.2 Sample preparation and system parameters

The initial granular sample is created by randomly placing 17 657 monodisperse particles inside a rectangular 3D box without overlap between them. The box size is $25d \times 25d \times 40d$. The compactness of the system can also be measured in terms of packing fraction ϕ, porosity $(1 - \phi)$, and void ratio e. The latter is defined as the ratio of pore volume to particle volume, so that[62]

$$e = \frac{1}{\phi} - 1. \qquad (10)$$

Void ratio is more commonly used in soil mechanics where the volume of the particles does not change during compaction, providing therefore a reference volume for the void space.[2,30,63,64] With this definition, $e = 1$ corresponds to equal volumes of particles and pores and a solid fraction $\phi = 0.5$. In our compaction simulations, the initial void ratio is $e_i = 1/\phi_i - 1 \simeq 1.72$, corresponding to $\phi = \phi_i \simeq 0.37$.

Isotropic compaction was applied by imposing the same pressure p on all six walls of the box. The gravity is set to zero to keep the sample in an isotropic stress state. Under the action of p, the walls move inward, compressing the particles until a stable mechanical equilibrium is reached. The simulation is stopped when the ratio of the kinetic energy to the total elastic energy stored in the contacts is 2×10^{-7}. This process is fully dynamic and depends not only on the initial void ratio e_0 but also on the wall mass m_w. The pressure p is kept constant, the force acting on each wall decreases as pS, where S is the surface area of the wall. The initial dynamics of compaction is governed by the acceleration pS/m_w. In most simulations used for scaling the void ratio with respect to system parameters, we kept e_i constant and m_w was set equal to 96 times the mass m of a single particle. However, further simulations were run for several different values of e_i and m_w to assess their effect on the resulting void ratios (see Section 3).

As the walls move inward, they collide with particles and we may distinguish two limit scenarios depending on the dissipation rate or adhesion force between particles. In one limit, the walls sweep and capture the particles and a densification front propagates from the walls towards the center of the simulation box. In the other limit, they push the particles away and the induced kinetic agitation leads to bulk aggregation of the particles. In both cases, the initial aggregation stage is followed by particle rearrangements under the action of compressive pressure. This second stage may fully erase the memory of the initial aggregation stage if the pressure is sufficiently high or the adhesion force is sufficiently small. Then, the initial void ratio e_i will not affect the resulting bonding structure and porosity of the packing. Otherwise, the compressive pressure is not high enough to destroy the bonding structure created by aggregation and the initial void ratio will fully determine the bonding structure. Fig. 2 displays an example of a jammed configuration and its bonding structure at the end of compaction. The force chains are composed of both compressive and tensile forces.

To enhance the randomness of particle positions, we added a small initial velocity $v_k = 10^{-3}$ m s^{-1} of random orientation to all particles. This kinetic energy is rapidly dissipated in the initial stages of compaction. The initial kinetic pressure $p_k = \rho\phi v_k^2$ is 57 times smaller than our lowest pressure $p_0 = 0.01$ MPa. Nevertheless, for this pressure, the walls are initially pushed outwards. Hence, the void ratio e increases beyond e_i and the subsequent aggregation under load leads to a slightly higher void ratio $e_0 \simeq 1.76$ ($>e_i = 1.72$) while the pressure is too low to induce further particle rearrangements. In the opposite case of high compressive pressure and low adhesion, we obtain the lowest void ratio e_{min}, which coincides with that of a packing of cohesionless
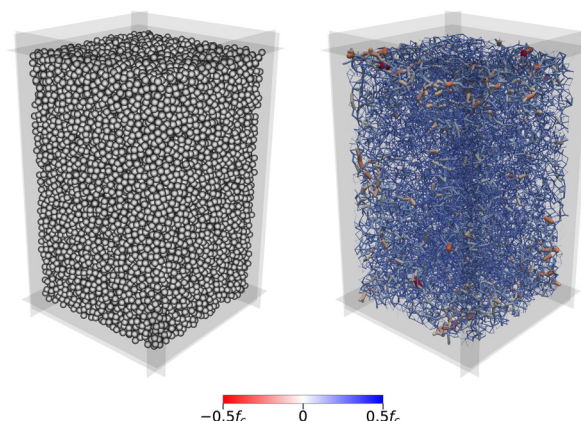

$-0.5f_c \qquad 0 \qquad 0.5f_c$

Fig. 2 3D representation of a jammed configuration and its bonding structure. Line thickness and color level are proportional to normal force with compressive (positive) forces in blue and tensile (negative) forces in red.

frictional particles. We obtain $e_{\min} \simeq 0.76$ ($\phi \simeq 0.57$) in agreement with previous studies.[65] All values of e reached during compaction vary therefore between $e_{\min}$ and e_0.

The two limits of compaction and the two stages of evolution of porosity can be clearly distinguished as shown in Fig. 3, which displays the evolution of e and the coordination number Z with time for several values of the cohesive stress $\sigma_c = f_c/d^2$ and p. At low pressure (dotted lines), e declines with time only at low cohesive stress; otherwise, it slightly increases as a result of the expansion of the simulation box before decreasing again to a constant value when all particles are aggregated. In this regime, the time needed for aggregation decreases as σ_c is increased. Note that Z continues to increase slowly as a result of rearrangements even when e reaches a nearly constant value. At high pressure (solid lines), the initial aggregation is fast and Z jumps from the very beginning to a finite value. e declines much faster for all values of adhesion force and we observe a slow evolution of Z even when e levels off. In all cases, the compaction stems from the combined effects of diffusion, aggregation and compression.

We performed compaction simulations with different values of the cohesive stress $\sigma_c = f_c/d^2$, the applied pressure p, and the

(a)

(b)

Fig. 3 Evolution of the void ratio e (a) and coordination number Z (b) as a function of time for three values of cohesive stress $\sigma_c = f_c/d^2$ and two values of pressure p.

Table 1 Values of system parameters used in this work

Parameters	Values
Cohesive stress σ_c [MPa]	11 values $\in [2 \times 10^{-3}, 4 \times 10^2]$
Pressure p [MPa]	4 values $\in [10^{-2}, 1]$
Elastic stress σ_e [MPa]	5 values $\in [5 \times 10^2, 2 \times 10^5]$
η	$[2.5 \times 10^{-3}, 4 \times 10^4]$
η^*	$[3.5 \times 10^{-5}, 31.6]$

elastic stress $\sigma_e = k_n/d$. The latter represents the order of magnitude of the elastic moduli of jammed configurations.[66] To vary σ_c, we varied the values of both f_c and d. For dimensional reasons, the particle size is irrelevant and, as we shall see, the void ratio is controlled by only two dimensionless variables that can be defined from the above three parameters. The ranges of the values of these parameters are given in Table 1. All other parameters are kept constant in most simulations. In particular, we set $m_w/m = 96$ and $\mu = 0.4$. The influence of wall mass m_w/m is considered separately in Section 3. The initial void ratio e_i is also likely to influence the aggregation phase and its influence is investigated in Section 3.

We initially performed 220 simulations with all combinations of the parameters mentioned in Table 1 and constant values of all other parameters. This corresponds to the number of data points used for the scaling of the void ratio. We ran 55 more simulations to assess the effect of the damping parameter α_n, 8 more simulations for the effect of wall mass m_w, and 8 other simulations for the influence of the initial void ratio e_i. In the following, e refers only to the void ratio of the final stable configuration obtained by isotropic compaction.

3 Scaling of porosity

In this section, we are interested in the effect of system parameters on the void ratio e of stable packings obtained by compaction with the goal of identifying dimensionless scaling parameters that control e.

3.1 Parametric study

Fig. 4(a) shows e as a function of pressure p for different values of cohesive stress σ_c and a fixed value of σ_e. As expected, the void ratio declines with increasing pressure. Furthermore, since adhesion tends to hinder particle rearrangements, higher cohesive stress leads to a larger void ratio. Fig. 4(b) shows e as a function of σ_c for different values of p and a fixed value of σ_e. We identify three phases in the evolution of e in agreement with the previous studies.[49,51] At low adhesion, e increases slowly with p from $e_{\min}$. As adhesion further increases, e increases more rapidly at a rate increasing with pressure. Finally, at even higher levels of adhesion, e tends to level off to a plateau value $e_{\max}$. The value of $e_{\max}$ declines as the pressure increases. As discussed previously, the highest value of e in our simulations is $e_0 = 1.76$, corresponding to the highest adhesion and lowest pressure $p_0 = 0.01$ MPa. The occurrence of a plateau suggests that a minimum value of σ_c is required to freeze the contact network in a configuration that is stable enough to withstand
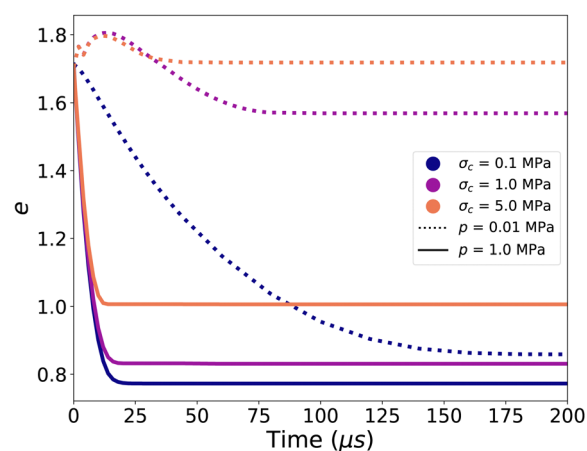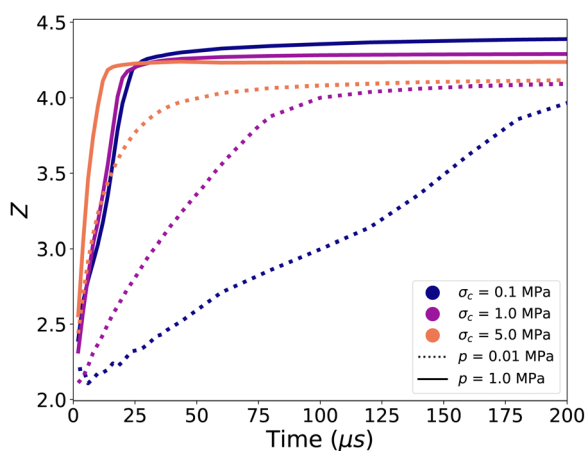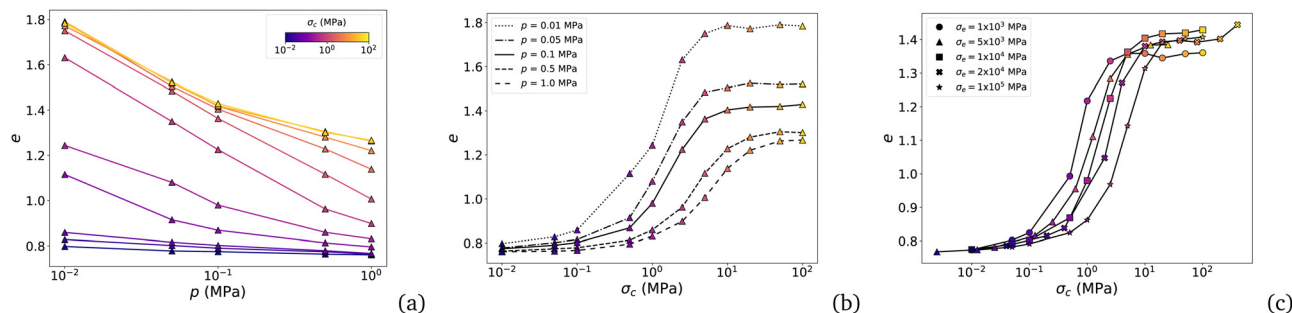
Fig. 4 Void ratio e of the stable packing obtained by compaction as a function of (a) applied pressure p for different values of cohesive stress σ_c and fixed values of σ_e; (b) σ_c for different values of the applied pressure p and fixed value of σ_e; (c) σ_c for different values of elastic stress σ_e and fixed value of p. The fixed values of applied pressure and elastic stress are $p = 0.1$ MPa and $\sigma_e = 10^4$ MPa, respectively.

rearrangements under the action of a given value of p. The increase of σ_c beyond this value is ineffective.

Fig. 4(c) shows e as a function of σ_c for different values of $\sigma_e = k_n/d$ and a fixed value of p. We see here a clear dependence of the void ratio on the contact stiffness. As σ_e increases, the same level of compaction occurs for higher values of σ_c. We also observe that e_{max} depends only slightly on σ_e. These effects of σ_e are not quite intuitive since particle stiffness is generally irrelevant to the rheology of cohesionless granular materials. This point will be discussed in more detail below in connection with the scaling of porosity.

A key question is whether the void ratio can be scaled with respect to dimensionless parameters combining the parameters σ_c, p, and σ_e. Dimensional analysis yields two independent dimensionless parameters, $\sigma_c/p = f_c/pd^2$ and $p/\sigma_e = pd/k_n$. Equivalently, the parameters $\sigma_c/\sigma_e = f_c/k_n d$ and $p/\sigma_e = pd/k_n$ may be considered. Given the mass m_w of the walls, we may also consider the ratio m_w/m as a third dimensionless parameter of the system. Hence, it might be possible to express the void ratio as an additive or multiplicative combination of these three parameters. The product of arbitrary powers of σ_c/p, p/σ_e, and m_w/m provides a simple function:

$$s = \left(\frac{\sigma_c}{p}\right)^a \left(\frac{p}{\sigma_e}\right)^b \left(\frac{m_w}{m}\right)^c, \quad (11)$$
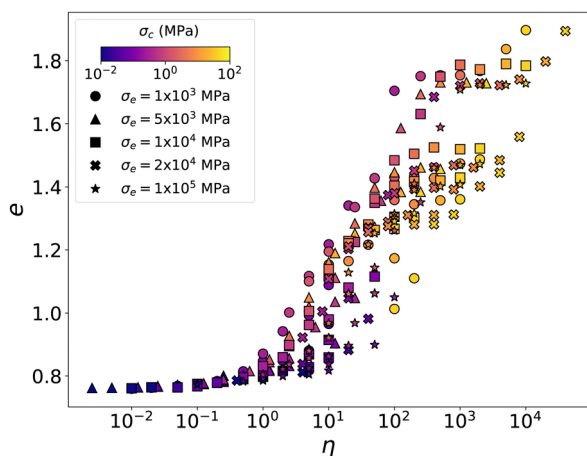
where a, b, and c are three exponents that depend on the mechanisms governing the compaction process. Only the ratios b/a and c/a of the exponents being mathematically meaningful for this scaling law, we set $a = 1$.

By setting $b = 0$ and $c = 0$, we obtain the cohesion number,

$$\eta = \frac{\sigma_c}{p} = \frac{f_c}{pd^2}, \quad (12)$$

which is a measure of the relative values of the cohesive stress and the compressive pressure p induced by the confining pressure.[64] Its inverse, called reduced pressure, has been used to scale packing fraction in previous studies in which k_n was set to a constant value.[22,49,67] Fig. 5 shows e as a function of η for all our compaction simulations and a fixed value of $m_w/m = 96$. We see that in the dense regime below $\eta = 1$, the data points collapse well as a function of η. Above $\eta = 1$, we observe a general trend of e to increase, but the data points are highly dispersed. This shows that e does not reflect only the condition of static equilibrium, which basically involves the balance of the pressure-induced force pd^2 with the adhesion force f_c, but it depends also on the dynamic process of compaction, which involves k_n in addition to f_c and p.

We find that the data points are much better regrouped together when b is set to a nonzero value. Considering mainly the points in the intermediate range of values of e, the best fit was obtained by setting $b = 1/2$ in eqn (11). The corresponding scaling parameter is

$$\eta^* = \frac{\sigma_c}{\sqrt{p\sigma_e}} = \frac{f_c}{\sqrt{pk_n d^3}}. \quad (13)$$

The void ratio and packing fraction are plotted as a function of this modified cohesion number η^* in Fig. 6. We see that the data points are now structured in several well-separated curves that differ in their plateau levels corresponding to different values of e_{max} or ϕ_{min}. The plateaus are well-defined except for a few datapoints that are either above (resp. below) or below (resp. above) the plateau of e (resp. ϕ) at high values of η^*. These datapoints are discussed in connection with rigid wall effects. For the definition of the plateau, we refer to the value $e = e_{max}$ or $\phi = \phi_{min}$ reached at $\eta^* \simeq 1$.

We also observe that the differences between different datasets in the intermediate range reflect their differences in
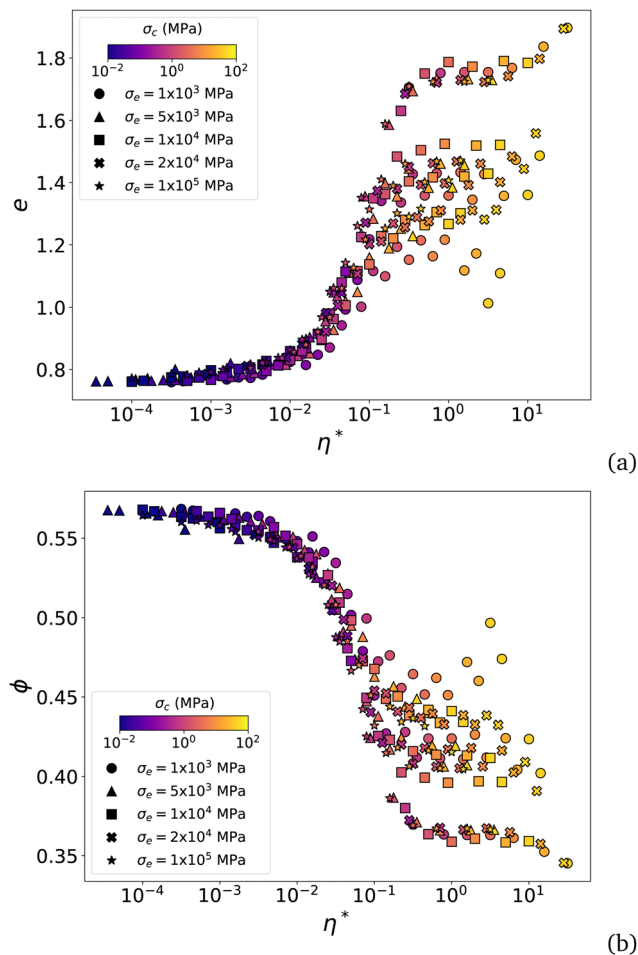

Fig. 5 Void ratio e as a function of cohesion number η. Each data point represents an independent compaction with parameter values represented by symbols and colors.

Fig. 6 Void ratio e (a) and packing fraction (b) as a function of modified cohesion number η^*. Each data point represents an independent compaction with parameter values represented by symbols and colors.

plateau levels e_{max}. The values of e_{max} can be extracted from the plots of void ratios as a function of p for different values of σ_c and σ_e. The plateau corresponds to the range of pressures $p < p^{crit}$ with

$$p^{crit} = \frac{\sigma_c^2}{\sigma_e}. \tag{14}$$

Note that the right-hand quantity is the order of magnitude of the cohesive energy per unit volume stored in the bond network. In other words, the plateau level e_{max} is reached when the applied pressure is not too high to cause plastic rearrangements for given values of σ_c and σ_e.

Fig. 7(a) displays e_{max} as a function of p^{crit}. The data points are rather well collapsed and fitted to a logarithmic function:

$$e_{max} = e_{min} + \frac{\Delta e}{1 + C \Delta e \ln(p^{crit}/p_{\Delta})}, \tag{15}$$

where C is a constant and p_{Δ} is the pressure for which $e_{max} = e_{min} + \Delta e$. For the fit shown in Fig. 7(a), we set $\Delta e = 1$ for which we have $p_{\Delta} = 0.01$ MPa and $C \simeq 0.24$. This value of p_{Δ} is the lowest pressure p_0 we employed. For this value of p_{Δ}, we obtain
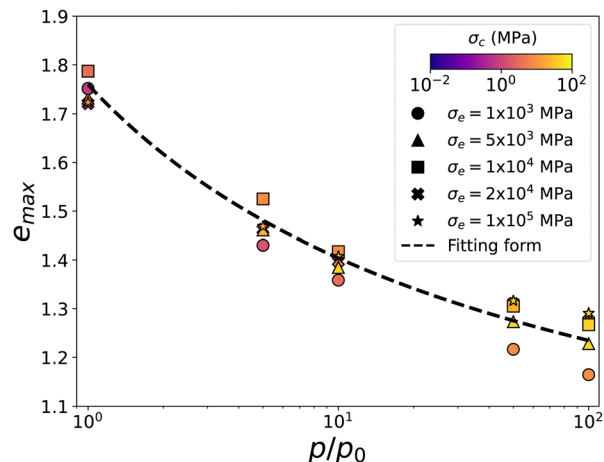

Fig. 7 The upper bound values e_{max} of void ratio (plateau levels) as a function of pressure $p = p^{crit} = \sigma_c^2/\sigma_e$ normalized by the lowest pressure p_0, corresponding to void ratio $e_0 \simeq 1.76$, for different sets of system parameters. The dashed line is the logarithmic fitting function of eqn (15).

$e_{max} = e_{min} + 1 \simeq 1.76$. Note also that $e_{min} \simeq 0.76$ corresponds to the highest packing fraction $\phi = 0.57$.

Eqn (15) predicts e_{max} in a unique way and independently of the choice of p_{Δ}. It is easy to show that this requirement is indeed satisfied if Δe and p_{Δ} satisfy the following relationship:

$$\Delta e = \frac{1}{1 + C \ln(p_{\Delta}/p_0)}. \tag{16}$$

For example, for $p_{\Delta} = 10p_0$, we obtain $\Delta e \simeq 0.64$ from eqn (16) and, according to eqn. (15), we have $e_{max} \simeq e_{min} + 0.64 = 1.4$ for $p = 0.1$ MPa. This value of e_{max} agrees well with the data of Fig. 7. Note also that C determines the curvature of the functional form and its value is independent of the choice of the reference pressure p_{Δ}.

We now can rescale the data points of Fig. 13 by considering the relative void ratio e_r defined from e_{min} and e_{max}:

$$e_r = \frac{e - e_{min}}{e_{max} - e_{min}}. \tag{17}$$

It varies from 0 for $e = e_{min}$ to 1 for $e = e_{max}$. Fig. 8(a) displays e_r as a function of η^*. We observe an excellent collapse of the data on a master curve, implying that e_r is a well-defined function of η^* which combines all our system parameters. A similar collapse naturally occurs for the packing fraction, as shown in Fig. 8(b), for the relative packing fraction $\phi_r = (\phi - \phi_{min})$-$(\phi_{max} - \phi_{min})$. Interestingly, this scaling makes a few datapoints clearly appear, marked in Fig. 8(a), that lie either slightly above or slightly below the plateau, revealing two limit conditions that will be discussed below.

This collapsed form of the porosity data and the presence of data points escaping the general trend raise several questions that will be further discussed below: (1) how to interpret the expression of the modified cohesion number η^* in eqn (13)? (2) Is the intermediate range of porosities best fit to a logarithmic function as often suggested by compaction experiments and simulations? (3) What is the effect of the damping
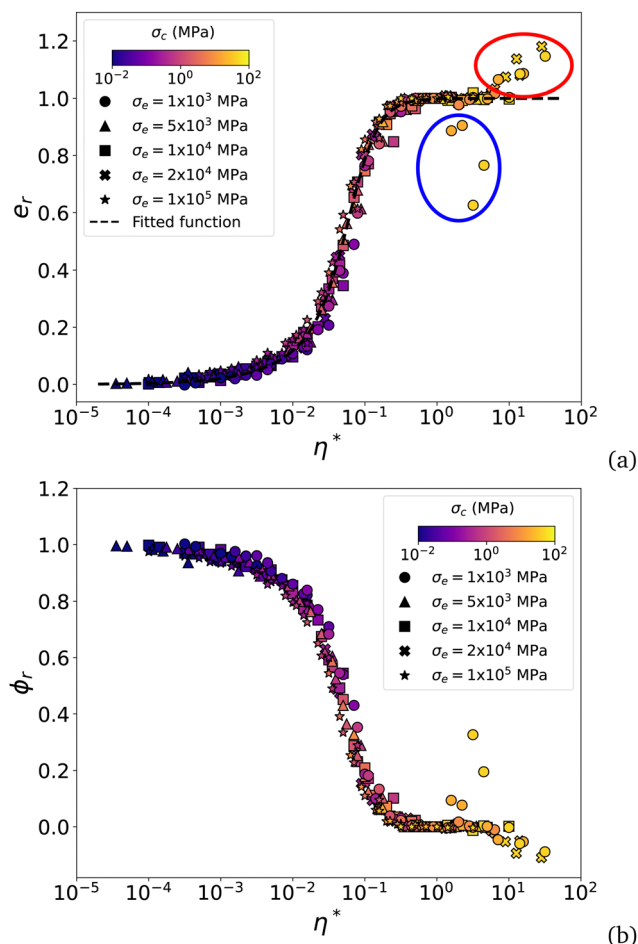
Fig. 8 Relative void ratio e_r (a) and relative packing fraction ϕ_r (b) as a function of the modified cohesion number η^* for the data obtained from all compaction simulations. The dotted line represents the fitting function given by eqn (31). The encircled symbols are the data points escaping the general scaling.

parameter α_n? (4) What are the effects of the wall mass m_w and initial void ratio? (5) What is the origin of deviating data points?

3.2 Modified cohesion number

The cohesion number η represents the relative importance of the cohesive stress σ_c acting at all contact points with respect to the pressure p in static equilibrium. However, compaction under load is a dynamic process and the porosities of the jammed configurations arise from the balance of energy rates such as in the thermodynamic description of the propagation and arrest of cracks in a solid material.[68] We may attribute a surface energy of the order of $G = f_c^2/(k_n d^2)$ to each contact. During compaction, particle rearrangements occur if this energy is overcome by the work $W = pd$ supplied by the action of p per unit surface and over a distance of the order of the particle size. Hence, the ratio $G/W = f_c^2/(p k_n d^3) = \sigma_c^2/(p \sigma_e) = (\eta^*)^2$ is expected to control the compaction level, *i.e.* the void ratio at which the particles get jammed in a stable configuration. The modified cohesion number η^* is the square root of this ratio. Hence, η^*

can be considered as a measure of the relative level of inertia during compaction. For this reason, we expect that for low values of η^*, where dynamic effects are less important, the void ratio is also well scaled by η, and this is what we observe in Fig. 5.

The effect of the attraction force on the dynamics can be analyzed in a more straightforward way by considering the collision of a particle with a rigid wall.[55] The equation of motion of the particle is given by:

$$m\ddot{\delta}_n = -k_n \delta_n - 2\alpha_n \sqrt{k_n m}\dot{\delta}_n - f_c \qquad (18)$$

where δ_n is the distance between the wall and the particle. Considering that upon collision at time $t = 0$ we have $(\delta_n(t = 0) = 0)$ and the particle has an impact velocity of $v_0 \left(\dot{\delta}_n(t = 0) = -v_0\right)$, the solution of eqn (18) is given by:

$$\delta_n(t) = \exp^{-t/\tau_2}(A\cos(t/\tau_1) + B\sin(t/\tau_1)) - A \qquad (19)$$

with

$$A = -\delta_c = \frac{f_c}{k_n}, \qquad (20)$$

$$B = \tau_1 \left(\frac{2f_c}{\sqrt{k_n m}}\alpha_n - v_0\right), \qquad (21)$$

$$\tau_1 = \frac{1}{(1 - \alpha_n^2)}\sqrt{\frac{m}{k_n}}, \qquad (22)$$

$$\tau_2 = \frac{1}{\alpha_n}\sqrt{\frac{m}{k_n}}. \qquad (23)$$

The evolution of δ_n follows a typical linear-spring-dashpot movement with the equilibrium position $\delta_n = \delta_c$.

Depending on the impact velocity v_0, two different scenarios occur. If v_0 is relatively low, the particle will stick to the wall and δ_n tends to δ_c after a few damped oscillations. Otherwise, the contact will open up and the particle rebounds with a lower velocity. The contact duration τ_c in this case satisfies the condition $\delta_n(\tau_c) = 0$, which can be shown to be equal to the solution of the following implicit equation:

$$e^{-\tau_c/\tau_2}\cos(\tau_c/\tau_1 - \gamma) = \cos(\gamma) \qquad (24)$$

with

$$\gamma = \arctan\left\{\tau_1\left(2\alpha_n\sqrt{\frac{k_n}{m}} - \frac{k_n v_0}{f_c}\right)\right\} \qquad (25)$$

Since the breakage of the contact should happen during the first period of the elastic bounceback ($\tau_c/\tau_1 < \gamma$), eqn (24) implies $\gamma > 0$. This leads to the following criterion for contact opening:

$$v_0 > v_{crit} = 2\alpha_n \frac{f_c}{\sqrt{k_n m}}. \qquad (26)$$

From the critical velocity v_{crit}, we can define a critical adhesion force in the case of compaction under load p:

$$f_c^{crit} = \frac{\sqrt{k_n m}v_0}{2\alpha_n} = \frac{\sqrt{p k_n d^3}}{2\alpha_n}, \qquad (27)$$

where we have set $v_0 = \sqrt{pd^3/m}$ as the typical velocity induced by the force pd^2 on particles. The critical adhesion force represents the adhesion force above which the particles stick together and aggregate. Obviously, compaction is not a binary process since the particle velocities are unevenly distributed. However, f_c^{crit} provides a reference adhesion force from which we can define a dimensionless adhesion force,

$$\frac{f_c}{f_c^{crit}} = 2\alpha_n \frac{f_c}{\sqrt{pk_n d^3}} = 2\alpha_n \eta^*, \qquad (28)$$

which is expected to be a control parameter of the compaction dynamics. Up to the damping coefficient, which is kept constant in our simulations, this ratio is the same as η^*. Its derivation from binary collisions sheds a new light on the role of η^* as a parameter that accounts for the probability of aggregation. In the previous argument based on the ratio of elastic energy release rate and the work of external forcing, the accent was on the likelihood of rearrangements. The aggregation and rearrangements are, however, two facets of the compaction process, which involves both loss and gain of contacts, as well as collective motion and deformation of aggregates. The critical velocity below which the effective restitution coefficient vanishes despite the nonzero value of the nominal restitution coefficient is an important dynamic effect of adhesion, which explains why the void ratio is not simply scaled by η. Based on this analysis, it can be conjectured that if the compaction is incremental and the particles are allowed the dissipation of their energy to reach static equilibrium after each increment of compressive pressure, η will provide an appropriate parameter and the void ratio will not depend on the contact stiffness.

3.3 Effect of wall mass and initial void ratio

In all simulations analyzed for the scaling of void ratio, the mass ratio m_w/m and initial void ratio e_0 were fixed to a constant value. We ran more simulations by varying separately these parameters for low and high values of p and σ_c. Fig. 9 displays the evolution of void ratio e as a function of time for a
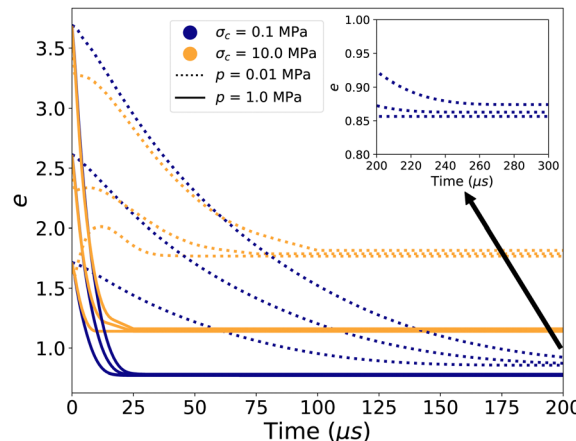
Fig. 10 Void ratio e as a function of time for 3 different values of the initial void ratio e_0, 2 different values of cohesive stress σ_c, and 2 different values of pressure p. The inset shows the long-time evolution of e in the case $p = 0.01$ MPa.

constant initial void ratio e_0, but three different values of m_w/m, two very different values of σ_c, and two very different values of p. We see that except for a small variation (without trend) at low p and high σ_c, the mass ratio has no effect on the final value of the void ratio. Hence, we must set $c = 0$ in the scaling law (11). This absence of wall mass effects, at least in the range of the investigated range of mass ratios, means that the kinetic energy acquired by the walls during compaction is efficiently dissipated as a result of inelastic collisions and formation of cohesive bonds.

Fig. 10 displays the evolution of e as a function of time for three different values of the initial void ratio, two different values of cohesive stress σ_c, and two different values of pressure p. We observe a clear effect of the initial void ratio on the compaction process, but the final void ratio is nearly independent of the initial void ratio. As in the case of wall mass, the kinetic energy acquired by the walls during compaction is rapidly dissipated since e decays monotonically and tends asymptotically to its equilibrium value, which is solely controlled by p, σ_c, and σ_e.

3.4 Fitting forms

Let us turn now to the functional form of the collapsed data $e_r(\eta^*)$ in Fig. 8. The intermediate range of this plot looks like a logarithmic function. However, as can also be checked in past simulations reported in the literature, this range actually concerns only a small part of the whole range of the values of η^*, which covers at least 5 orders of magnitude. A power law has also been suggested in the dense regime ($e_r < 0.2$).[23,24] We found no fit in the literature for the loose regime ($e_r > 0.8$). In 2D simulations of compaction with samples prepared by aggregation, the upper plateau is not reached as an asymptotic state and the crossover between the intermediate and loose regimes is discontinuous since it reflects a transition from stable aggregates to collapsed aggregates. However, previous 3D simulations based on the same preparation process do show a gradual transition to the loose state as in our simulations of Fig. 8.[50,51]
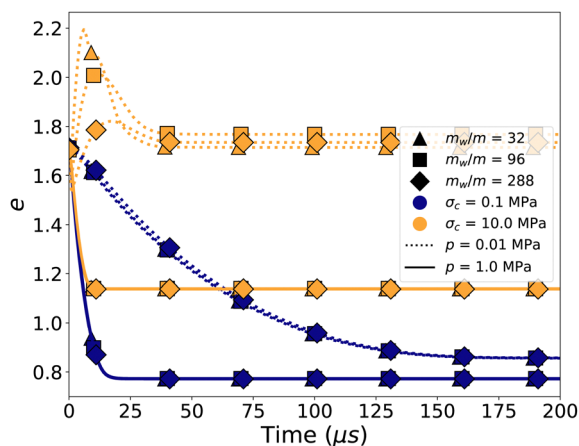

Fig. 9 Void ratio e as a function of time for 3 different values of the ratio m_w/m of wall mass to particle mass, 2 different values of cohesive stress σ_c, and 2 different values of pressure p.
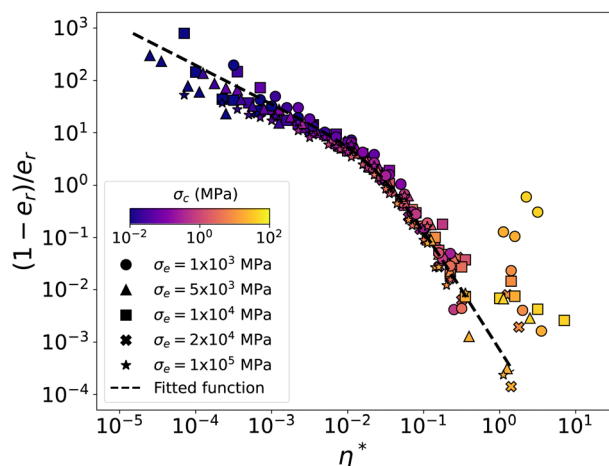
Fig. 11 Rescaled data of the relative void ratio e_r as a function of scaling parameter η^*.

The trend in this intermediate-to-loose crossover observed in Fig. 8 is similar to that of the dense-to-intermediate crossover, but there is an obvious asymmetry between them. In particular, the evolution of e_r in the dense regime is slow and takes place over several decades whereas in the loose regime, it occurs for less than one decade. To make clearly appear this difference, let us consider the ratio

$$s \equiv \frac{1 - e_r}{e_r} = \frac{e_{\max} - e}{e - e_{\min}}, \tag{29}$$

which compares the differences between e from its maximum and minimum values. It is plotted in Fig. 11 as a function of η^*. We see that the data are divided into two regimes, each plausibly described by a power law. In fact, a single fitting function excellently describes the whole range of data:

$$s = \frac{1}{A\left(\eta^*/\eta_m^*\right)^\alpha + \left(s_m^{-1} - A\right)\left(\eta^*/\eta_m^*\right)^\beta}, \tag{30}$$

with $A \simeq 0.475$, $\alpha \simeq 0.74$, and $\beta \simeq 2.3$. The point with coordinates $\eta^* = \eta_m^* \simeq 0.045$ and $s = s_m \simeq 1.55$ is the crossover point. This representation suggests that the intermediate logarithmic regime is practically absent and simply reflects the transition between the two power-law regimes. Interestingly, a similar power-law behavior with $\alpha = 3/4$ for the dense regime was found by contact dynamics simulations of dynamic

compaction in 2D.[24] However, the effect of contact stiffness was not included in the scaling proposed and all the data were described as a function of η.

From eqn (30), we get the following fitting form for $e_r(\eta^*)$:

$$e_r = \frac{A\left(\eta^*/\eta_m^*\right)^\alpha + \left(s_m^{-1} - A\right)\left(\eta^*/\eta_m^*\right)^\beta}{1 + A\left(\eta^*/\eta_m^*\right)^\alpha + \left(s_m^{-1} - A\right)\left(\eta^*/\eta_m^*\right)^\beta}. \tag{31}$$

This functional form is plotted in Fig. 8(a) together with the simulation data. We see that it provides an excellent fit for the relative void ratio as a function of the modified cohesion number. In this fit, the ratio/captures the asymmetry of the curve. This asymmetry may depend on the initial void ratio e_i, mass ratio m_w/m and whether the compaction pressure is applied incrementally or not.

3.5 Effect of damping parameter

All the void ratio data discussed so far were obtained from simulations with a fixed value of dissipation parameter $\alpha_n = 0.25$. However, eqn (28) naturally suggests $\alpha_n \eta^*$ as a scaling parameter rather than η^*. The issue is therefore whether α_n can be included in a simple way in the scaling of void ratios. To assess the effect of α_n, we ran a series of simulations with different values of α_n while also varying σ_c for $p = 0.1$ MPa and $\sigma_e = 10^4$ MPa. The results are shown in Fig. 12(a). As expected, for each value of η^*, e increases with α_n because of the stabilizing effect of energy dissipation or, equivalently, because of the decrease of the effective restitution coefficient or increase of the critical velocity, as suggested by eqn (26). This effect is most pronounced for intermediate values of η^*. In transition to the plateau, the effect of α_n declines since the stabilizing effect of f_c prevails in this regime. For the same reason, $e_{\max}$ is independent of α_n.

If, as suggested by eqn (28), we plot the same data as a function of $\alpha_n \eta^*$, we obtain Fig. 12(b). We see that the data collapse indeed in the dense regime, but the discrepancy increases everywhere else. The best collapse is obtained by using the scaling parameter $\alpha_n^{1/4} \eta^*$ as shown in Fig. 12(c). Data collapse is nevertheless mediocre in the dense regime. Note that a dependence on $\alpha_n^{1/4}$ was observed in shear localization.[52,53] The same authors found a scaling of cohesion with $\alpha_n^{0.7}$ in a different problem.[53] It seems therefore that the void ratio depends in a nonlinear and unmonotonic way on the level of adhesion. Further simulations are necessary to arrive at
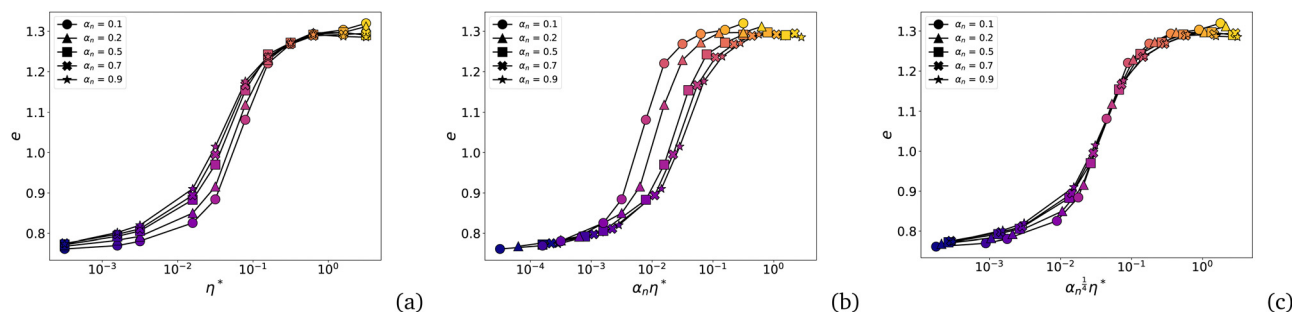

Fig. 12 Evolution of void ratio e as a function of η^* (a), $\alpha_n \eta^*$ (b), and $\alpha_n^{1/4} \eta^*$ (c), for different values of damping parameter α_n.

a scaling that includes the dissipation parameter. This can be done by investigating the influence of α_n on the general shape of $e_r(\eta^*)$, *i.e.* by quantifying the dependence of the parameters of the functional form of eqn (31) on α_n.

4 Bonding structure

Particle configuration, contact network and force transmission are key features that evolve during the compaction process. Besides porosity, these features underlie mechanical properties and functionalities for which compaction is used in industry. For example, while the void ratio is essential for the transport of fluid in the pore space, the contact network underlies the electronic and heat conductivity across a packing. The pore and solid phases are, however, related together through two constraints: (1) geometrical duality of the particle and pore phases, and (2) force balance at the level of each particle. A fundamental issue is therefore whether the void ratio and variables pertaining to the bonding structure are correlated across the parametric space, *i.e.* in the whole range of values of compressive pressure, contact adhesion, and contact stiffness. Hence, we consider in this section, several aspects of the bonding structure and investigate their scaling with system parameters.

4.1 Force networks

Fig. 13 displays three examples of the bond network with increasing value of the modified cohesion number η^*. At low cohesion (Fig. 13(a)), nearly all force chains are in the compressive state. Although it is difficult to fully appreciate the force chains in a 3D perspective, the strongest forces are clearly located in the vicinity of the walls, featured by several arches along the walls or spanning the space between adjacent walls in the corners of the box. Such wall effects are common in cohesionless packings and their presence together with a small gradient of forces from the walls towards the center of the box indicate that mesoscopic force inhomogeneities occur in our system on top of the well-known particle scale force inhomogeneity.[60,69–73]

At higher cohesion (Fig. 13(b)), we observe both compressive and tensile force chains. The void ratio is higher but a higher density of forces occurs at the corners of the box. We also see that the number of particle–wall contacts is reduced, implying that the transmission of the applied pressure from the walls to the sample is concentrated over a few contacts. At an even higher level of cohesion (Fig. 13(c)), the network is even looser and the tensile and compressive forces are almost equally present everywhere.

Fig. 14 displays the bond networks for one data point of each of the two groups of data escaping the general scaling in Fig. 8. The first group, encircled in red in Fig. 8, occurs at lowest pressures ($p \leq 5.10^{-2}$ MPa) and the data points are above the plateau $e_r = 1$. Fig. 14(a) is an example of the corresponding bonding network. As a result of very low pressure and high adhesion, the particles fully aggregate before the wall moves and comes in contact with only a few particles. The higher porosity of these samples is in agreement with 3D quasi-static compaction simulations.[51]

The second group, encircled in blue in Fig. 8, occurs at very high pressures ($p \geq 0.5$ MPa) and high cohesive stress. Fig. 14(b) shows an example of the corresponding bonding network. High pressure leads to the fast creation of stable and strong force chains along the walls followed by their buckling. As a result, most particles in the bulk are screened and receive a small amount of external pressure. The high density in a thick layer close to the walls leads to a lower global void ratio. Such inhomogeneous structures at low and high pressure in highly cohesive granular materials show the effect of both wall dynamics and finite sample size on the compaction process. In particular, high pressures lead to fast motion of the walls and dynamic jamming, tending to enhance force correlations and giving rise to stable arches across the system.

To better characterize the bonding structure for the 'regular' and 'deviating' data points, we calculated the void ratio as a function of the distance r from the center of the samples. To do so, we calculated the void ratios inside a cubic probe of side $2r$ and centered on the center of the sample. Fig. 15 shows e as a

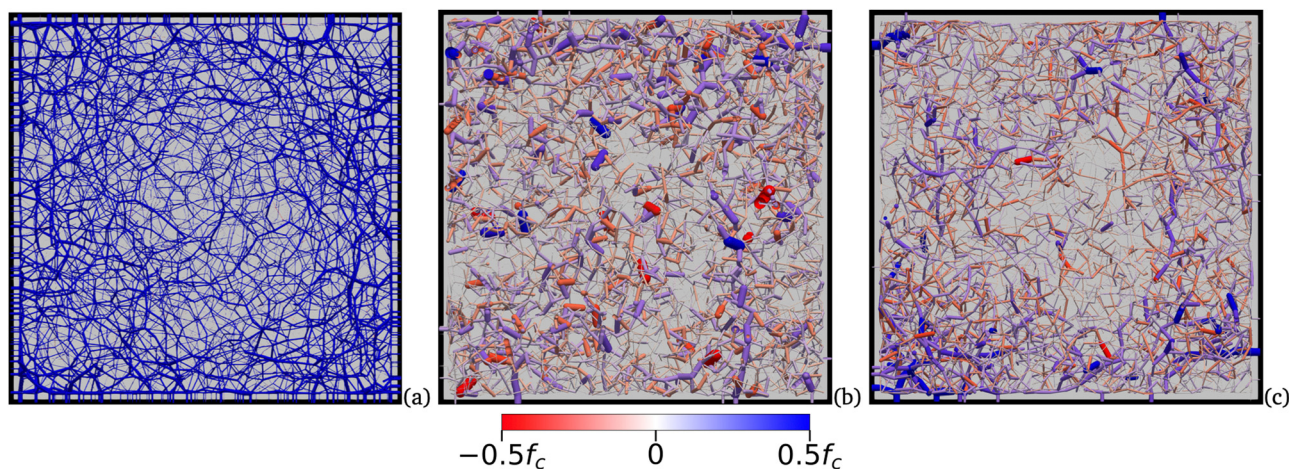

$-0.5f_c$ 0 $0.5f_c$

Fig. 13 Force network in a thin slice inside the packing for (a) $\eta^* = 10^{-3}$, (b) $\eta^* = 0.05$, and (c) $\eta^* = 0.5$. Line thickness is proportional to force magnitude.
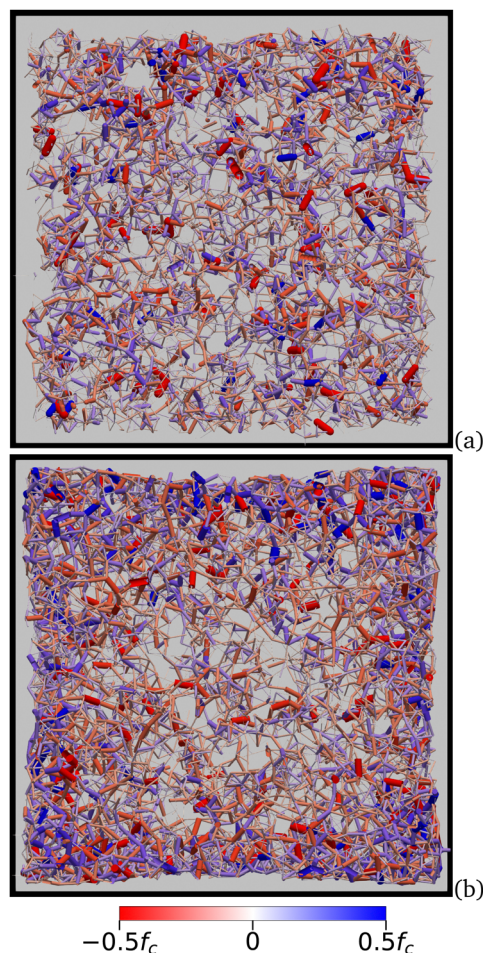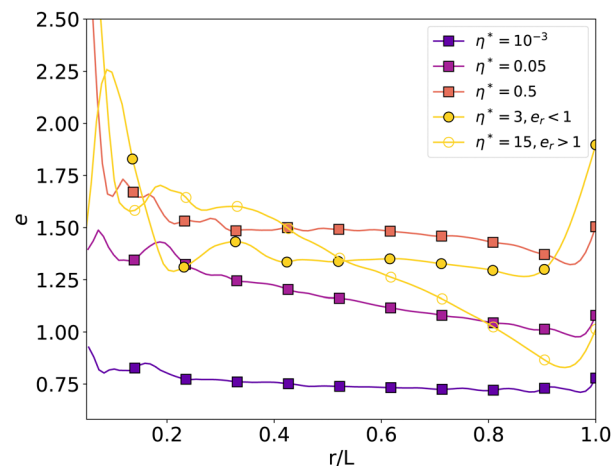
Fig. 15 Void ratio e in a cubic probe with side $2r$ and the same center as the sample as a function of r/L, where L is the length of the sample, for $\eta^* = 10^{-3}$ (corresponding to Fig. 13(a)), $\eta^* = 0.05$ (corresponding to Fig. 13(b)), $\eta^* = 0.5$ (corresponding to Fig. 13(c)), $\eta^* = 15$ (corresponding to Fig. 14(a)), and $\eta^* = 3$ (corresponding to Fig. 14(b)).

Fig. 14 Force network in a thin slice inside the packing for (a) $\eta^* = 15$, $e_r > 1$ and (b) $\eta^* = 3$, $e_r < 1$. Line thickness is proportional to the force magnitude.

4.2 Coordination numbers

The coordination number Z is the lowest-order scalar variable characterizing the contact network. We find that in all packings and independently of system parameters, Z varies between 4 and 4.2. Since the coordination number of an isostatic frictional packing of spheres is 4, this means that bonding structures are only weakly hyperstatic even in the dense regime and the force networks are almost uniquely defined. A similar result was found by compaction simulations with 3D periodic boundary conditions.[51] The contact network is therefore fragile in the sense that, although it is globally stable, it can easily break or undergo large deformations under the action of shear stresses. The fact that Z remains low throughout the parametric space indicates that low coordination is a consequence of isotropic compaction, which is common to all our simulations. Higher levels of coordination can be reached by shearing or for soft deformable particles.

Since Z does not discriminate the generated packings, we consider tensile and compressive contacts whose numbers vary with the level of cohesion as observed in Fig. 13. Let Z^+ and Z^- be the compressive and tensile coordination numbers, *i.e.* the average numbers of compressive contacts ($f_n > 0$) and tensile contacts ($f_n < 0$), respectively. We have $Z = Z^+ + Z^-$. Fig. 16 shows both Z^+ and Z^- as a function of η^* and η with all simulation compaction data points. We see that Z^- increases steadily with η and levels off around 2 at large values of η while at the same time Z^+ declines and tends to the same value of 2. Hence, in the asymptotic state, each particle has 2 tensile contacts and 2 compressive contacts on average. This symmetry between the tensile and compressive networks in the asymptotic state reflects the fact that at large values of η the force network (with its both tensile and compressive contacts) is mainly induced by adhesion forces which are well above the forces induced by the confining pressure.[74]

function of r/L, where L is the sample size. The five curves correspond to the five bond networks of Fig. 13 and 14. In all cases, we observe a higher void ratio in the center of the sample and in the vicinity of the walls. The observed oscillations in the center reflect the local ordering of particles or cohesive aggregates due to steric exclusions. Between these two limits, we observe either a plateau (for $\eta^* = 0.5$) or a small gradient for the regular data points (for $\eta^* = 10^{-3}$ and $\eta^* = 0.05$). For the deviating points, we observe either a strong gradient (case of $\eta^* = 15$ with $e_r > 1$) or a very high void ratio at the wall (case of $\eta^* = 3$ with $e_r < 1$). These pathologies reflect therefore a strong finite size effect in the former case and a strong wall effect in the latter case. In this latter case, we also see that the oscillations of e extend from the center to mid-distance from the wall, indicating the presence of aggregates, as can also be observed in Fig. 14(b). The finite-size effects are naturally expected in the case of highly cohesive granular materials due to the clustering of cohesive particles. We find it interesting that the general scaling of e_r with η^* occurs despite such effects and porosity gradients inside the samples.
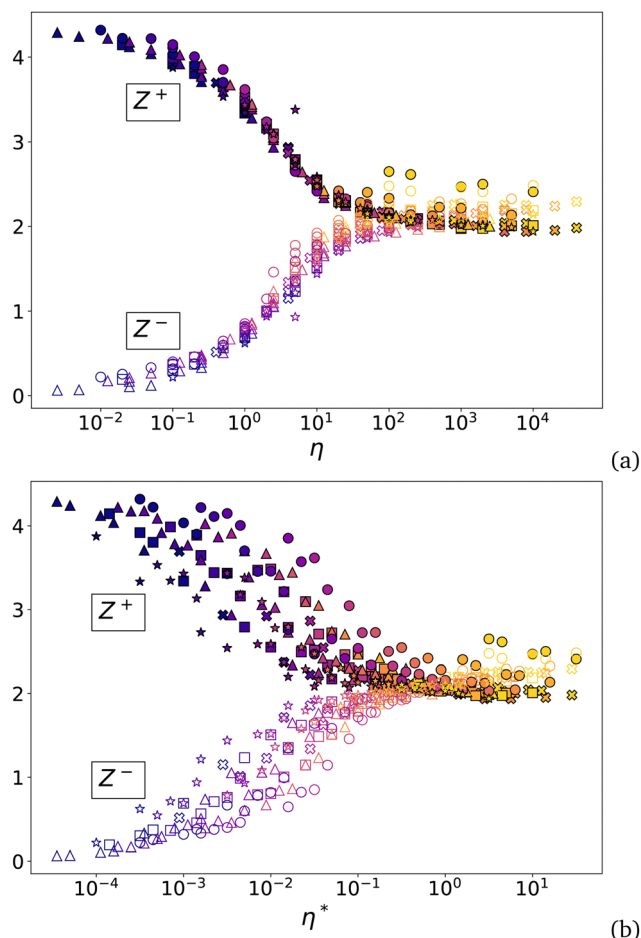
Fig. 16 Evolution of the coordination numbers Z^- (empty symbols) and Z^+ (plain symbols) as a function of η and η^*. The symbols and colors are the same as in Fig. 8.

Remarkably, in contrast to the void ratio, the coordination number data collapse much better as a function of η rather than η^*! This means that, since $\eta^* = \sqrt{\eta}\sqrt{\sigma_c/\sigma_e}$, the same values of Z^+ and Z^- for a fixed value of η are compatible with a range of values of void ratio obtained by simply changing σ_e. This is quite important for the range of intermediate values of e_r where the latter changes significantly with η^*. Fig. 17 shows e_r as a function of the proportion Z^-/Z of tensile contacts. We see that for each value of Z^-/Z (depending on η), e_r varies indeed in a broad range of values with the widest variation occurring just before the plateau. We also see that the largest (resp. lowest) values of e_r correspond to the lowest (resp. largest) values of σ_e. Fig. 18 shows force networks for $\eta = 10$ but with different values of σ_e. We clearly see that the force gradient increases from the center towards the walls with increasing relative void ratio e_r although the distributions of tensile and compressive contacts are similar in the three networks.

The scaling of compressive and tensile coordination numbers with η rather than η^*, although unexpected, is actually a consequence of static equilibrium. This equilibrium is ensured at the level of each particle by the balance of forces induced by
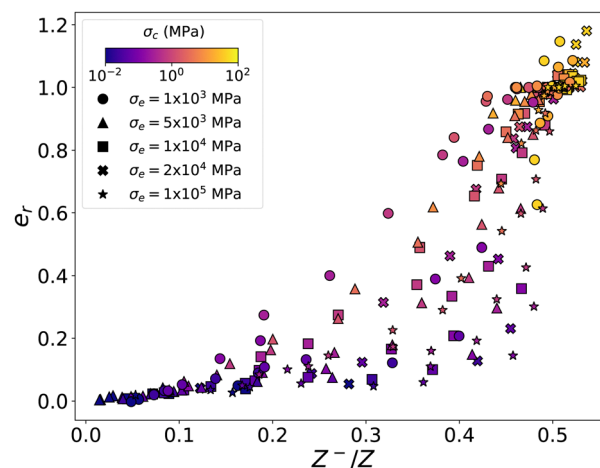

Fig. 17 Relative void ratio e_r as a function of the proportion Z^-/Z of tensile contacts for all simulations.

the applied pressure, which is of the order of pd^2, and the adhesion forces f_c acting at all contacts. The connectivity of the contact network characterized by Z being nearly the same for all compacted configurations, it is plausible that the force network characterized by the proportion Z^-/Z of tensile contacts depends on the relative importance of adhesion force and applied pressure *via* the ratio $\eta = f_c/pd^2$.

4.3 Force distributions

The bonding structure can be analyzed in more detail by considering the probability density function (PDF) of normal forces f_n. As f_c is the reference internal force which varies in our parametric study, we focus on the distribution of force ratios f_n/f_c. Since we have $f_n = f_n^e - f_c$ at every contact point, the force ratio is $f_n/f_c = f_n^e/f_c - 1$ so that the PDF of force ratios actually represents the statistics of the mobilization of repulsive forces in the bond network as compared to the adhesion force. Fig. 19 shows three examples of the PDFs of normalized forces f_n/f_c. For the three values of η^*, we observe a double-exponential distribution:

$$P(f_n) \propto \begin{cases} e^{\beta^- f_n/f_c} & \text{for } f_n \leq 0, \\ e^{-\beta^+ f_n/f_c} & \text{for } f_n \geq 0, \end{cases} \quad (32)$$

characterized by the exponents $\beta^- > 0$ and $\beta^+ > 0$ for the ranges of tensile and compressive forces, respectively. These exponents describe the width of the distribution in the two ranges, which change with η^*. We also observe a Dirac peak at $f_n = 0$ when adhesion is low. Similar distributions have been reported in the past and the Dirac peak was attributed to the interface between particles or regions of mean positive (compressive) and mean negative (tensile) pressures.[74]

We computed the values of β^- and β^+ in the ranges $[-0.5f_c, 0]$ and $[0, 1.5f_c]$ for which we generally have sufficient statistics. The precision is low in the range of tensile forces at low values of η due to a much lower number of tensile forces. Fig. 20 shows β^- and β^+ as a function of both η and η^*. Consistently with the behavior of Z^- and Z^+ and within our
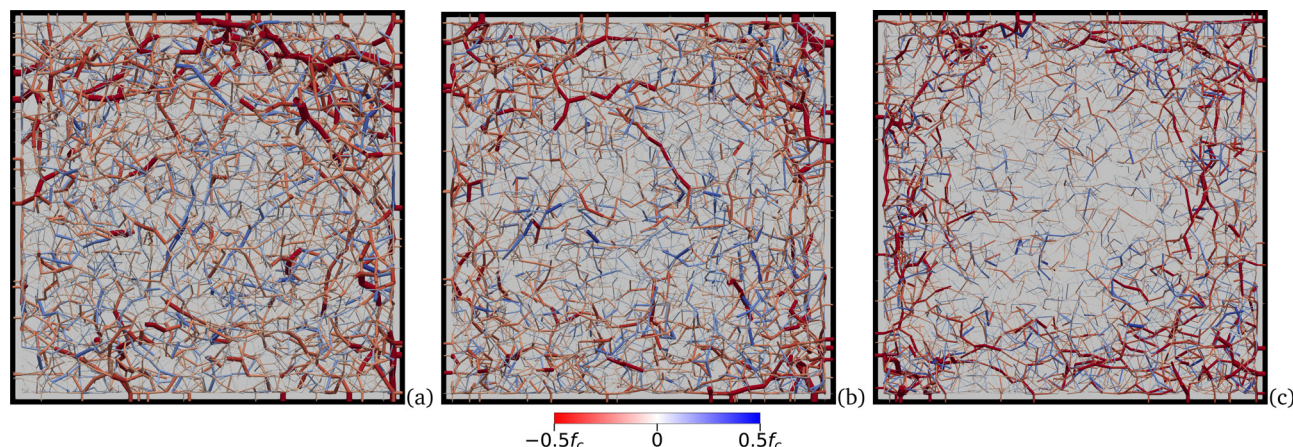
Fig. 18 Force networks in a thin slice inside the packing for $\eta = 10$ and $e_r = 0.1$ (a), $e_r = 0.5$ (b), and $e_r = 0.9$ (c).
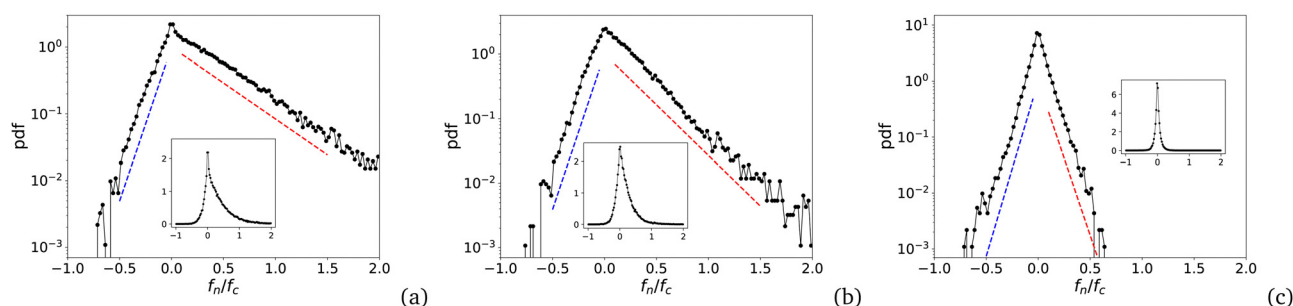

Fig. 19 Probability density function of normal force f_n normalized by adhesion force f_c for (a) $\eta^* = 10^{-3}$, (b) $\eta^* = 0.05$, and (c) $\eta^* = 0.5$. The dashed lines are a guide to eyes for a purely exponential function.

statistical precision, we find that β^- and β^+ are much better scaled by η than η^*. Hence, as in the case of Z^-/Z, the force distributions are increasingly uncoupled from the relative void ratio as η increases. Interestingly, both β^- and β^+ first decrease and then increase again at larger values of η. The initial decrease is more pronounced for β^+. The minimum value occurs at $\eta \simeq 0.2$ ($e \simeq 0.8$) and, according to Fig. 6, it corresponds to the transition from the dense regime to the intermediate regime. The two exponents tend to have the same value at large η.

To understand the unmonotonic evolution of the exponents with η, it must be reminded that the evolution of the force PDF reflects the effect of adhesion on the distribution of elastic forces $f_n^e = -k_n\delta_n$. In the dense regime, the effect of increasing adhesion is to reinforce strong force chains via weak tensile forces that play in this way the same role with respect to the strong force network as the weak compressive forces.[75] As a result, the number of strong compressive forces and the inhomogeneity of the force network increase, the force PDFs become wider, and β^+ declines. Beyond $\eta \simeq 0.2$, the tensile network grows and self-sustained groups of particles mixing compressive and tensile forces appear as observed in Fig. 13(b). The amplitude of strong compressive forces is increasingly dictated by the adhesion force rather than external pressure. As a result, the scale of the compressive force is increasingly

imposed by σ_c rather than p and the value of β^+ tends to that of β^-. In this sense, the force network becomes more symmetric around $f_n = 0$ with equal numbers of tensile and compressive forces.

The observed behavior of the exponents indicates a fundamental asymmetry between the effects of confining pressure and adhesive forces on the equilibrium of granular packing. This point is not trivial when a variable such as η is used as a control parameter, suggesting that the pressure p and compressive stress σ_c play identical roles with respect to the equilibrium of the force network. In fact, in the limit where the confining pressure p prevails ($\eta \ll 1$), the PDF $P_1(f_n/pd^2) \propto e^{\beta' f_n/pd^2}$ of normalized normal forces is independent of p (i.e. β' does not depend on p). When $\eta \gg 1$ and the effect of adhesion prevails, f_c is the relevant force scale and $P(f_n/f_c)$ is independent of f_c (i.e. β^+ does not depend on f_c). Statistically, the crossover from the regime ruled by p to the regime ruled by f_c occurs when the probabilities for the two alternative normalizations are equal: $P_1(f_n/pd^2)\delta f_n/pd^2 = P(f_n/f_c)\delta f_n/f_c$. Given the exponential form of the PDFs, this condition translates into $\beta^+ f_n/f_c = \beta' f_n/pd^2$, which implies $\beta^+ \simeq \eta\beta'$. The value of β' can be evaluated at $\eta = 1$, where $f_c = pd^2$ and therefore $\beta^+ = \beta'$. Fig. 20 shows that at this point we have $\beta^+ \simeq 1$, implying $\beta' \simeq 1$. Since β' does not depend much on p in this limit, we may assume that its value remains equal to 1 for lower
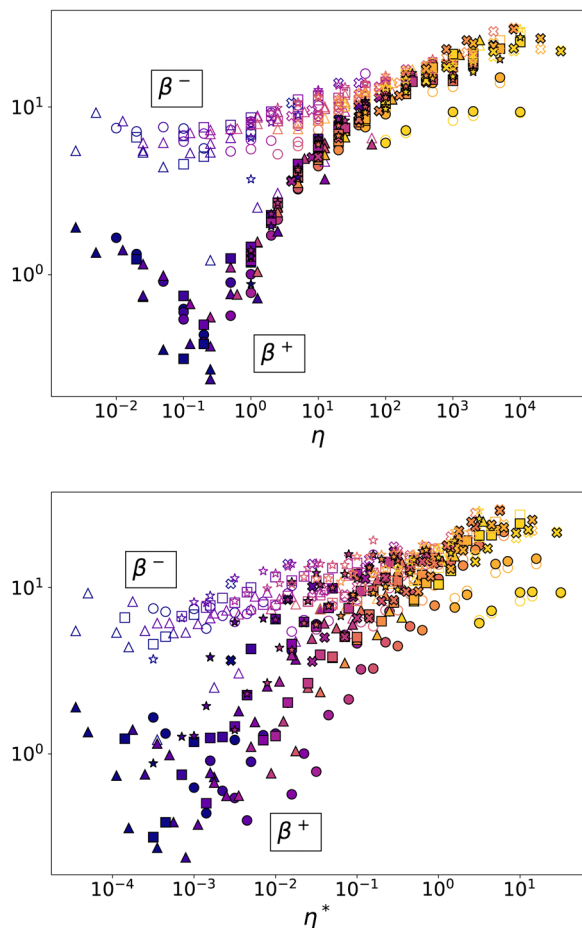
Fig. 20 Evolution of the exponents β^- (empty symbols) and β^+ (plain symbols) of the force PDFs for the tensile and compressive force domains. The symbols and colors are the same as in Fig. 8.

values of η. Hence, at the crossover between the two regimes, we have $\beta^+ = \eta\beta' \simeq \eta$. Fig. 20(a) shows that this condition holds with a good approximation at $\beta^+ \simeq 0.2$, which corresponds to the minimum of the curve.

5 Conclusions

Particle dynamics simulations were performed to investigate the scaling of porosity and structural characteristics with system parameters in cohesive granular materials assembled under the action of an isotropic compressive pressure. Spherical particles governed by linear elasto-adhesive and frictional interactions were used in the simulations for broad ranges of values of cohesive stress, contact stiffness, compressive pressure, and particle size. In contrast to previously reported simulations, the compaction process in our simulations is fully dynamic due to the action of the applied compressive pressure. Because of the initially non-overlapping configuration of particles, this process involves ballistic aggregation, dynamic jamming, and particle rearrangements before a stable packing in static equilibrium is reached. In this work, the adhesion force was assumed to represent the vdW interactions. However, the

results hold also for other types of cohesive materials provided that the attraction force is short-ranged and localized at the contact point and the cohesive stress σ_c can be clearly defined from the nature of the interaction. For example, liquid-bonded contacts in the limit of low liquid volume fraction are characterized by a short debonding distance (nearly equal to the cubic root of liquid volume) and a maximum capillary force proportional to the liquid–gas surface energy at the contact point.[76,77]

A key finding is the scaling of the relative porosity (or relative void ratio) with a new dimensionless parameter η^* which combines pressure p, cohesive stress σ_c, and characteristic elastic stress σ_e. It was argued that this modified cohesion number arises naturally by considering that, as in fracture mechanics, particle rearrangements depend on the work supplied by the applied pressure as compared to the elastic energy stored in the contact network. This scaling was also related to the critical velocity of aggregation between colliding adhesive particles. Particle stiffness appears therefore as a control parameter of dynamic compaction as it was previously found for fluidization and shear banding in cohesive granular materials. We also found that the initial void ratio and wall mass have no influence on the void ratio obtained by compaction under constant pressure.

The scaling of void ratio e with system parameters is complex essentially due to the fact that there are three independent variables (p, σ_e, and σ_c) and the evolution of e is nonlinear with two plateaus involving the parameters $e_{\min}$, which is determined mainly by the geometry of the particles, and $e_{\max}$, which is itself a function of system parameters. It is therefore useful to formulate the dependence of e on system parameters as a "recipe". The recipe is actually simple if we concentrate on only one variable. Let us consider, for example, the evolution of e with p for fixed values of σ_c and σ_e. As p increases from zero, $\eta^* = \sigma_c/\sqrt{p\sigma_c}$ declines, but e remains constant and equal to $e_{\max}$ until $p = p^{\mathrm{crit}} = \sigma_c^2/\sigma_e$ is reached. For values of p exceeding p^{crit}, the void ratio e declines with increasing p (decreasing η^*). When we plot e_r, defined from the value of $e_{\max}$ obtained by this procedure, as a function of η^*, we obtain a normalized plot as the one shown in Fig. 8(a) but restricted to the given values of σ_c and σ_e. Our main finding is that all the curves obtained by this procedure for all other values of σ_c and σ_e collapse on a master curve of sigmoidal shape. In each dataset, the values of σ_c, σ_e and $e_{\max}$ are different. Hence, we must also clarify how $e_{\max}$ depends on σ_c and σ_e.

For any given values of the two latter parameters, if a sufficiently low pressure is applied (below p^{crit}), we have $e = e_{\max}$. This dependence is expressed through the combination $p^{\mathrm{crit}} = \sigma_c^2/\sigma_e$. When $e_{\max}$ is plotted as a function of p^{crit}, the data points nearly collapse as in Fig. 7. This is a decreasing function that has a nearly logarithmic form. However, we are not allowed to use a dimensional quantity such as p^{crit} inside the logarithm function. A possible solution for normalizing p^{crit} consists in using an arbitrary pressure p_Δ as the reference point provided the fitting form is independent of its value. Eqn (15) represents $e_{\max}$ as a function of $p^{\mathrm{crit}}/p_\Delta$ with $p_\Delta = p_0$, which is the lowest

value that we had used in the simulations. For this value, we have $\Delta e \simeq 1$. However, we showed that eqn (15) is invariant with respect to the choice of p_Δ, each value of the latter corresponding to a unique value of Δe. Taking p_0 as a reference point, we have $C \simeq 0.24$ and $\Delta e = 1/[1 + C \ln(p_\Delta/p_0)]$. Any choice of the values of Δ_e and p_Δ in eqn (15) satisfying this relation leads to the same value of $e_{\max}$ for given values of σ_c and σ_e. In other words, the predicted value of $e_{\max}$ by eqn (15) does not depend on the choice of p_0 as the reference pressure.

The functional dependence of void ratio on η^* was shown to be best fit by a general form involving two power laws for (1) the increase of void ratio from the lowest porosity in the limit ruled by pressure and (2) the asymptotic increase of void ratio towards its highest value in the limit ruled by adhesion forces. Furthermore, the asymptotic void ratio is a function of critical pressure depending on cohesive stress and elastic stress. We showed that the effect of the damping parameter on porosity depends on the level of adhesion and can not be included in a simple way in the general scaling proposed. We also discussed the origins of a few data points escaping the proposed scaling and showed that they stem either from a slow motion of the walls and full ballistic aggregation of the particles due to very low pressure applied or from a fast inward motion of the walls due to very high pressure applied, causing dynamic jamming and high porosity gradients inside the packing. In both cases, the presence of the walls and the finite size of the sample as compared with force correlations play a crucial role. An important finding of this work is that, despite such effects, the overall void ratio follows a well-defined scaling with η^* within the limits that were discussed, clarified, and illustrated.

The bonding structure was analyzed in terms of contact network connectivity, tensile/compressive networks, and force PDFs. These features were found to scale with the cohesion number $\eta = \sigma_c/p$ rather than η^*. This implies the remarkable property that a given force distribution is compatible with a wide range of values of void ratio. This variability reflects the effect of the characteristic elastic stress σ_e on the assembling process and increases with η. For all values of η, the coordination number Z is only slightly above 4, which is the isostatic coordination number for frictional spheres, showing therefore the weak hyperstaticity of the packings generated by isotropic compaction. The PDFs of both tensile and compressive forces are generically exponential with exponents that vary unmonotonically with η, revealing a transition from the dense regime, characterized by the stabilizing effect of adhesion, to the loose regime, mainly controlled by adhesion forces. As η increases, the bond network tends to have a symmetrical structure with similar PDFs and equal numbers of tensile and compressive forces.

Our results prove that granular materials can be assembled by dynamic compaction in packings of high void ratio with only normal adhesion forces and no need for rolling resistance. Previous simulations have shown that high levels of void ratio can not be reached by quasi-static incremental compression without rolling friction or without allowing the particles to aggregate freely before the application of the compaction pressure.[23] Our simulations may be considered as primary compaction to build a granular sample since the initial state is a granular gas. It will therefore be interesting to perform dynamic compaction simulations starting from a different state (e.g. the loosest state of our simulations or a packing obtained by ballistic aggregation) and investigate the relevance of the modified cohesion number to the scaling of porosity.

It is also important to consider the effect of Hertzian contacts for which the characteristic elastic stress explicitly depends on the pressure. It can be conjectured that the scaling proposed in this paper based on the elastic stress as an independent parameter will hold true by replacing the elastic stress with bulk modulus, which explicitly depends on the confining pressure in the case of a Hertz contact.[78] This will then modify the expression of η^*. Another significant parameter is the friction coefficient μ between particles. Its value was fixed to 0.4 throughout our parametric investigation. However, the effect of μ on the proposed scaling is nontrivial. In particular, it is interesting to see whether μ controls only the value of $e_{\max}$ without modifying the scaling or whether it has a more extensive influence on the compaction process. The aggregation of particles and force correlations inside the packings and their link with finite size effects and deviating data points were discussed in this paper, but more simulations are needed with increasing number of particles or simulation cell size to quantify such effects. Finally, we investigated the shear response of the packings obtained in this work with a focus on the evolution of the void ratio. The results will be published in an upcoming paper.

Author contributions

Max Sonzogni: data curation, formal analysis, investigation, methodology, software, visualization, writing – original draft. Jean-Mathieu Vanson: methodology, software, investigation, data curation, resources, writing – review and editing, supervision. Katerina Ioannidou: data curation, investigation, resources, supervision, writing – review and editing. Yvan Reynier: data curation, investigation, validation, writing – review and editing. Sébastien Martinet: data curation, investigation, validation, writing – review and editing. Farhang Radjai: conceptualization, data curation, formal analysis, investigation, methodology, resources, supervision, writing – original draft.

Conflicts of interest

The authors declare that they have no known competing financial interests or personal relationships that could have appeared to influence the work reported in this paper.

Acknowledgements

Notes and references

1 B. Andreotti, Y. Forterre and O. Pouliquen, *Granular Media: Between Fluid and Solid*, Cambridge University Press, 2013.

2 J. Mitchell and K. Soga, *Fundamentals of Soil Behavior*, Wiley, 3rd edn, 2005, p. 592.

3 J. C. Jaeger, N. G. W. Cook and R. Zimmerman, *Fundamentals of Rock Mechanics*, Wiley, 2007.

4 A. Adolfsson and C. Nyström, *Int. J. Pharm.*, 1996, **132**, 95–106.

5 M. Kadiri, A. Michrafy and J. Dodds, *Powder Technol.*, 2005, **157**, 176–182.

6 C.-Y. Wu, B. Hancock, A. Mills, A. Bentham, S. Best and J. Elliott, *Powder Technol.*, 2008, **181**, 121–129.

7 A. Mazor, L. Orefice, A. Michrafy, A. de Ryck and J. G. Khinast, *Powder Technol.*, 2018, **337**, 3–16.

8 G. Frenning, *Powder Technol.*, 2007, **172**, 103–112.

9 B. Saint-Cyr, J.-Y. Delenne, C. Voivret, F. Radjai and P. Sornay, *Phys. Rev. E: Stat., Nonlinear, Soft Matter Phys.*, 2011, **84**, 041302.

10 B. Saint-Cyr, F. Radjai, J.-Y. Delenne and P. Sornay, *Phys. Rev. E: Stat., Nonlinear, Soft Matter Phys.*, 2013, **87**, 052207.

11 P. N. Davies, H. E. Worthington, F. Podczeck and J. M. Newton, *Eur. J. Pharm. Biopharm.*, 2007, **67**, 268–276.

12 O. Keles, N. P. Barcenas, D. H. Sprys and K. J. Bowman, *AAPS PharmSciTech*, 2015, **16**, 1455–1464.

13 I.-H. Oh, N. Nomura, N. Masahashi and S. Hanada, *Scr. Mater.*, 2003, **49**, 1197–1202.

14 H. Shen, H. Li and L. Brinson, *Mech. Mater.*, 2008, **40**, 708–720.

15 L. Reig, C. Tojal, D. J. Busquets and V. Amigó, *Materials*, 2013, **6**, 4868–4878.

16 N. Nitta, F. Wu, J. T. Lee and G. Yushin, *Mater. Today*, 2015, **18**, 252–264.

17 H. Kang, C. Lim, T. Li, Y. Fu, B. Yan, N. Houston, V. De Andrade, F. De Carlo and L. Zhu, *Electrochim. Acta*, 2017, **232**, 431–438.

18 H. Liu, X. Cheng, Y. Chong, H. Yuan, J.-Q. Huang and Q. Zhang, *Particuology*, 2021, **57**, 56–71.

19 Y. Liu, R. Zhang, J. Wang and Y. Wang, *iScience*, 2021, **24**, 102332.

20 E. N. Primo, M. Chouchane, M. Touzin, P. Vazquez and A. A. Franco, *J. Power Sources*, 2021, **488**, 229361.

21 H. M. Jaeger, S. R. Nagel and R. P. Behringer, *Phys. Today*, 1996, **49**, 32–38.

22 P. G. Rognon, J.-N. Roux, D. Wolf, M. Naaïm and F. Chevoir, *Europhys. Lett.*, 2006, **74**, 644–650.

23 F. A. Gilabert, J.-N. Roux and A. Castellanos, *Phys. Rev. E: Stat., Nonlinear, Soft Matter Phys.*, 2007, **75**, 011303.

24 D. E. Wolf, T. Unger, D. Kadau and L. Brendel, *Powders and Grains 2005*, 2005, pp. 525–533.

25 V. Busignies, B. Leclerc, P. Porion, P. Evesque, G. Couarraze and P. Tchoreloff, *Eur. J. Pharm. Biopharm.*, 2006, **64**, 38–50.

26 A. Djemai and I. C. Sinka, *Int. J. Pharm.*, 2006, **319**, 55–62.

27 E. Andò, S. A. Hall, G. Viggiani, J. Desrues and P. Bésuelle, *Géotechnique Lett.*, 2012, **2**, 107–112.

28 J. C. Quezada, P. Breul, G. Saussine and F. Radjai, *PRE*, 2012, **86**, 031308.

29 N. Roy, J. D. Frost and G. Viggiani, *Granular Matter*, 2022, **24**, 63.

30 A. Schofield and P. Wroth, *Critical State Soil Mechanics*, McGraw-Hill Inc.,US, 1968, p. 310.

31 J. B. Knight, C. G. Fandrich, C. N. Lau, H. M. Jaeger and S. R. Nagel, *Phys. Rev. E: Stat., Nonlinear, Soft Matter Phys.*, 1995, **51**, 3957–3962.

32 L. J. Budinski-Petkovi and S. B. Vrhovac, *Eur. Phys. J. E: Soft Matter Biol. Phys.*, 2005, **16**, 89–96.

33 J. M. Valverde, A. Castellanos and M. A. Sanchez Quintanilla, *PRL*, 2001, **86**, 3020–3023.

34 J. M. Valverde, A. Castellanos and P. K. Watson, *Powder Technol.*, 2001, **118**, 236–241.

35 J. M. Valverde and A. Castellanos, *Granular Matter*, 2007, **9**, 19–24.

36 R. Cabiscol, H. Shi, I. Wünsch, V. Magnanimo, J. H. Finke, S. Luding and A. Kwade, *Adv. Powder Technol.*, 2020, **31**, 1280–1289.

37 C. J. Ridgway, K. Ridgway and G. P. Matthews, *J. Pharm. Pharmacol.*, 1997, **49**, 377–383.

38 M. A. S. Quintanilla, J. M. Valverde, A. Castellanos and R. E. Viturro, *PRL*, 2001, **87**, 194301.

39 F. Fichtner, A. Rasmuson and G. Alderborn, *Int. J. Pharm.*, 2005, **292**, 211–225.

40 E. Garzón, P. J. Sánchez-Soto and E. Romero, *Appl. Clay Sci.*, 2010, **48**, 307–318.

41 H. Mohammed, B. J. Briscoe and K. G. Pitt, *Powder Technol.*, 2006, **165**, 11–21.

42 Q. Ku, J. Zhao, G. Mollon and S. Zhao, *Powder Technol.*, 2023, **421**, 118455.

43 S. Nezamabadi, F. Radjai, J. Averseng and J.-Y. Delenne, *J. Mech. Phys. Solids*, 2015, **83**, 72–87.

44 P. A. Cundall and O. D. L. Strack, *Géotechnique*, 1979, **29**, 47–65.

45 T. Pöschel and T. Schwager, *Computational Granular Dynamics: Models and Algorithms*, Springer, 2005.

46 C. Thornton, *Granular Dynamics, Contact Mechanics and Particle System Simulations*, Springer International Publishing, 2015.

47 P. G. Rognon, J.-N. Roux, M. Naaïm and F. Chevoir, *J. Fluid Mech.*, 2008, **596**, 21–47.

48 F. Radjai and F. Dubois, *Discrete-element modeling of granular materials*, ISTE, 2011.

49 F. A. Gilabert, J.-N. Roux and A. Castellanos, *Phys. Rev. E: Stat., Nonlinear, Soft Matter Phys.*, 2008, **78**, 031305.

50 V.-D. Than, J.-N. Roux, A.-M. Tang and J.-M. Pereira, *E3S Web Conf.*, 2016, **9**, 08008.

51 V. D. Than, S. Khamseh, A. M. Tang, J.-M. Pereira, F. Chevoir and J.-N. Roux, *J. Eng. Mech.*, 2017, **143**, C4016001.

52 S. Mandal, M. Nicolas and O. Pouliquen, *Proc. Natl. Acad. Sci. U. S. A.*, 2020, **117**, 8366–8373.

53 S. Mandal, M. Nicolas and O. Pouliquen, *Phys. Rev. X*, 2021, **11**, 021017.

54 R. Moreno-Atanasio, B. Xu and M. Ghadiri, *Chem. Eng. Sci.*, 2007, **62**, 184–194.

55 T. Kobayashi, T. Tanaka, N. Shimada and T. Kawaguchi, *Powder Technol.*, 2013, **248**, 143–152.

56 V. Richefeu and P. Villard, *Modeling Gravity Hazards from Rockfalls to Landslides*, Elsevier, 2016, p. 161.

57 M. P. Allen and D. J. Tildesley, *Computer Simulation of Liquids*, Oxford University Press, 2017.

58 K. L. Johnson, K. Kendall and A. D. Roberts, *Proc. R. Soc. A*, 1971, **324**, 301–313.

59 R. Moreno-Atanasio, S. Antony and M. Ghadiri, *Powder Technol.*, 2005, **158**, 51–57.

60 F. Radjaï, I. Preechawuttipong and R. Peyroux, in *Cohesive granular texture*, ed. P. A. Vermeer, H. J. Herrmann, S. Luding, W. Ehlers, S. Diebels and E. Ramm, Springer Berlin Heidelberg, Berlin, Heidelberg, 2001, pp. 149–162.

61 N. V. Brilliantov, N. Albers, F. Spahn and T. Pöschel, *Phys. Rev. E: Stat., Nonlinear, Soft Matter Phys.*, 2007, **76**, 051302.

62 J. B. Burland, *Géotechnique*, 1990, **40**, 329–378.

63 D. M. Wood, *Soil Behaviour and Critical State Soil Mechanics*, Cambridge University Press, 1991.

64 A. Castellanos, *Adv. Phys.*, 2005, **54**, 263–376.

65 C. Song, P. Wang and H. Makse, *Nature*, 2008, **453**, 629–632.

66 D. C. Vu, L. Amarsid, J.-Y. Delenne, V. Richefeu and F. Radjai, *Granular Matter*, 2023, **26**, 6.

67 N. Berger, E. Azéma, J.-F. Douce and F. Radjai, *EPL*, 2015, **112**, 64004.

68 H. Laubie, F. Radjaï, R. Pellenq and F.-J. Ulm, *J. Mech. Phys. Solids*, 2017, **105**, 116–130.

69 F. Radjai, D. E. Wolf, M. Jean and J.-J. Moreau, *Phys. Rev. Lett.*, 1998, **80**, 61–64.

70 T. S. Majmudar and R. P. Behringer, *Nature*, 2005, **435**, 1079–1082.

71 V. Richefeu, F. Radjaï and M. S. El Youssoufi, *Eur. Phys. J. E: Soft Matter Biol. Phys.*, 2006, **21**, 359–369.

72 R. P. Behringer, K. E. Daniels, T. S. Majmudar and M. Sperl, *Philos. Trans. R. Soc., A*, 2008, **366**, 493–504.

73 F. Fazelpour and K. E. Daniels, *Soft Matter*, 2023, **19**, 2168–2175.

74 V. Richefeu, M. S. El Youssoufi, E. Azéma and F. Radjaï, *Powder Technol.*, 2009, **190**, 258–263.

75 F. Radjai, S. Roux and J. J. Moreau, *Chaos*, 1999, **9**, 544–550.

76 G. Lian, M. J. Adams and C. Thornton, *J. Fluid Mech.*, 1996, **311**, 141.

77 V. Richefeu, M. S. El Youssoufi, R. Peyroux and F. Radjaï, *Int. J. Numer. Anal. Methods Geomech.*, 2008, **32**, 1365–1383.

78 I. Agnolin and J.-N. Roux, *Phys. Rev. E: Stat., Nonlinear, Soft Matter Phys.*, 2007, **76**, 061304.